9-1-2009

Improved Confidence in (U-Th)/He Thermochronology Using the Laser Microprobe: An Example from a Pleistocene Leucogranite, Nanga Parbat, Pakistan

J. W. Boyce
Massachusetts Institute of Technology

K. V. Hodges
Massachusetts Institute of Technology

D. King
Carl Zeiss MicroImaging, Inc.

James L. Crowley
Boise State University

M. Jercinovic
University of Massachusetts

See next page for additional authors

Authors

J. W. Boyce, K. V. Hodges, D. King, James L. Crowley, M. Jercinovic, N. Chatterjee, S. A. Bowring, and M. Searle

Click Here for Full Article

Improved confidence in (U-Th)/He thermochronology using the laser microprobe: An example from a Pleistocene leucogranite, Nanga Parbat, Pakistan

J. W. Boyce

Department of Earth, Atmospheric, and Planetary Sciences, Massachusetts Institute of Technology, 77 Massachusetts Avenue, Cambridge, Massachusetts 02215, USA (jwboyce@alum.mit.edu)

Department of Earth and Space Sciences, University of California, 595 Young Drive East, Los Angeles, California 90095–1567, USA

K. V. Hodges

Department of Earth, Atmospheric, and Planetary Sciences, Massachusetts Institute of Technology, 77 Massachusetts Avenue, Cambridge, Massachusetts 02215, USA

School of Earth and Space Exploration, Arizona State University, Box 871404, Tempe, Arizona 85287, USA

D. King

Materials Research Division, Carl Zeiss MicroImaging, Inc., One Zeiss Drive, Thornwood, New York 10594, USA

J. L. Crowley

Department of Earth, Atmospheric, and Planetary Sciences, Massachusetts Institute of Technology, 77 Massachusetts Avenue, Cambridge, Massachusetts 02215, USA

Department of Geosciences, Boise State University, Mailstop 1535, 1910 University Drive, Boise, Idaho 83725-1535, USA

M. Jercinovic

Department of Geosciences, University of Massachusetts, 611 North Pleasant Street, Amherst, Massachusetts 01003–9297, USA

N. Chatterjee and S. A. Bowring

Department of Earth, Atmospheric, and Planetary Sciences, Massachusetts Institute of Technology, 77 Massachusetts Avenue, Cambridge, Massachusetts 02215, USA

M. Searle

Department of Earth Sciences, Oxford University, Parks Road, Oxford OX1 3PR, UK

[1] The newly developed laser microprobe (U-Th)/He thermochronometer permits, for the first time, the ability to generate precise (U-Th)/He cooling ages for even very young (<1 Ma) samples with a spatial resolution on the order of tens of micrometers. This makes it possible to test the reproducibility of independent (U-Th)/He age determinations within individual crystals, further increasing the reliability of the method. As an example, we apply it here to a Pleistocene granite from Nanga Parbat, Pakistan, where previous constraints on the thermal history are consistent with rapid exhumation and cooling. Twenty-one (U-Th)/He dates determined on two monazite crystals from a single granite sample yield a mean of

748,000 years with a ~95% confidence level of ±19,000 years. There is no discernible variation in the distribution of (U-Th)/He ages in the cores of these crystals and therefore no evidence for the development of substantial diffusive-loss ^{4}He zoning over 80% of the interior of the monazite crystals during postcrystallization cooling of the granite. Modeling of these data suggests that cooling at a mean rate of ~300 K/Ma would be necessary to produce the observed ages and the lack of a ^{4}He gradient, which is consistent with preexisting constraints for Nanga Parbat. Increased precision in thermochronology permits more tightly constrained exhumation models, which should aid geologic interpretation.

1. Introduction

[2] The (U-Th)/He geochronometer relies on the production of ^{4}He from naturally occurring ^{235}U, ^{238}U, ^{232}Th, and ^{147}Sm through alpha decay [e.g., *Farley*, 2002; *Reiners*, 2002]. Radiogenic ^{4}He diffuses rapidly in minerals at relatively low temperatures (<300°C) compared to the daughter products of chronometers such as U-Pb, Lu-Hf, and Sm-Nd, which typically record the time elapsed since crystallization. Thus, (U-Th)/He dates are usually interpreted as cooling ages, with each mineral assigned a closure temperature (T_C) corresponding to that age based on the cooling rate, the size of the grain (or its effective diffusion dimension), and the temperature-dependent diffusivity of ^{4}He in the mineral [*Dodson*, 1973]. The utility of the (U-Th)/He technique has been demonstrated for a wide range of applications, including meteorite chronometry, development of topography, tephrochronology, and most commonly determining the exhumation-induced cooling of samples in tectonically active regions [*Farley et al.*, 2000; *House et al.*, 1998; *Min*, 2005]. These studies have relied on whole-crystal or "conventional" (U-Th)/He age determinations, which often result in larger than expected systematic and random errors due to zoning and other unidentified complications [*Boyce and Hodges*, 2005; *Tagami*,

2003]. Generating large, statistically significant data sets requires the development of new methods to produce precise ages quickly. Furthermore, in many geologic settings, slow postcrystallization cooling will produce a ^{4}He concentration gradient in the grain, with a predicted topology that is related to the specific thermal history of the sample [*Dodson*, 1986]. Exploiting internal gradients for tectonic studies also requires new techniques that can quantify intracrystalline ^{4}He variations. The laser microprobe (U-Th)/He thermochronometer, implemented here on samples of an unknown (but under 1.5 Ma) age for the first time, can potentially address both of these issues.

[3] The fidelity of the laser microprobe (U-Th)/He technique [*Boyce et al.*, 2006] has been previously demonstrated on the MOM monazite standard (Ataleia, Minas Gerais, Brazil). Monazite is a rare earth element phosphate mineral, nominally CePO$_4$, but commonly enriched in U, Th, and Sm. These centimeter-sized, gem-quality monazite crystals have different, but internally invariant U, Th, and Sm concentrations, making them ideal for any number of in situ techniques (including (U-Th)/He), and to date have been employed as standards in a half-dozen electron probe and ion microprobe laboratories around the world. Conventional (U-Th)/He ages (449.6 ± 9.8 Ma, 2SE) and laser microprobe (U-Th)/He ages (455.3 ± 3.7 Ma, 2SE)
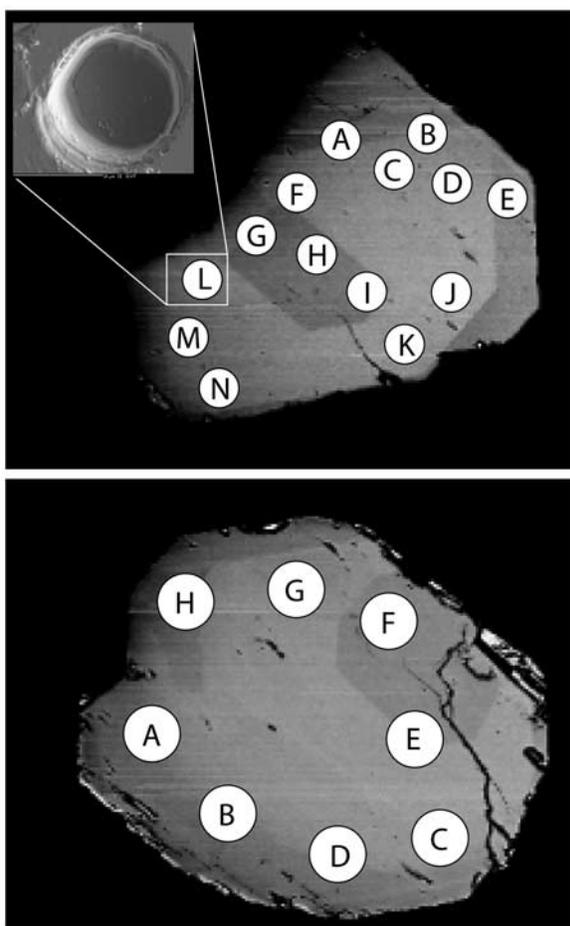
Figure 1. Backscattered electron (BSE) intensity maps of the two crystals from sample K94-34, depicting the similar zoning present in both crystals. White circles indicate locations of the ablation pits, which are ~30 μm in diameter and ~12–14 μm deep. The inset is a BSE image of an ablation pit. Scale bars in both images represent 100 μm and do not apply to the inset image.

agree within 1.3% for more than 30 total analyses on two different crystals. Given the general inability of (U-Th)/He laboratories around the world to reproduce any natural crystal standard to better than ~5% [*Boyce and Hodges*, 2005; *McDowell et al.*, 2005; M. van Soest, personal communication, 2008], this agreement confirms that the laser microprobe can be used to generate cooling ages that are as accurate as conventional (U-Th)/He ages. However, dating unzoned centimeter-scale gem-quality crystals that are several hundred million years old is a far cry from dating typical crystals which are small, zoned, broken, included and otherwise more difficult to work with, in addition to typically being younger and therefore having much lower radiogenic He concentrations.

Extending laser microprobe (U-Th)/He of monazite to such samples was the motivation of this study.

2. Nanga Parbat as a Test of (U-Th)/He Thermochronometry

[4] The Nanga Parbat-Haramosh region of Pakistan includes dramatic exposures of granitic and high-grade metamorphic rocks that record the development of very high geothermal gradients during the most recent stages of Himalayan orogenesis [*Craw et al.*, 1997; *Winslow et al.*, 1994]. Structural, geomorphic, and geochemical data suggest that surface uplift and rock exhumation rates of the Nanga Parbat massif over the past few million years may have been among the highest on Earth, resulting in local relief in excess of 7000 m and young cooling ages that are often within error of zero [*George et al.*, 1995; *Koons et al.*, 2002; *Treloar and Rex*, 1990; *Winslow et al.*, 1996; *Zeitler et al.*, 1982, 1989, 2001]. Nanga Parbat provides an ambitious test of the ability of the laser microprobe (U-Th)/He method to generate meaningful ages on very young samples.

3. Nanga Parbat Monazites

[5] In this study, we apply the laser microprobe (U-Th)/He method to monazite crystals from a biotite + cordierite + tourmaline leucogranite that crosscuts foliation in the host gneisses above Fairy Meadows camp, north of the summit of Nanga Parbat at an elevation of approximately 3500 m. Isotope-dilution, thermal ionization mass spectrometry U-Pb data for accessory minerals from this sample suggest crystallization ages of 1.2–1.4 Ma [*Crowley et al.*, 2005]. We would expect the (U-Th)/He cooling ages of these samples to be significantly younger than the U-Pb crystallization ages, even in the case of rapid exhumation.

[6] Two 250–300 μm diameter monazite crystals were prepared as described in detail below. Backscattered electron images of both crystals (Figure 1) display evidence for chemical zoning that corresponds to variations in U and Th concentration determined by electron microprobe analysis. Both crystals are fractured and included making them less than ideal candidates for conventional (U-Th)/He. Both crystals also have unusual shapes, and at least one of the two crystals (Figure 1, top) is incomplete, and would be difficult to correct for lost He due to alpha recoil [*Farley et al.*, 1996].

U, Th, and Sm concentrations were measured by electron microprobe at The University of Massachusetts, following procedures outlined by *Jercinovic and Williams* [2005]. Care was taken to correct U concentrations for overlap of the Th family of X-ray lines (Th M-g, Th M3-N4, the associated high-energy M3-N4 satellite, and Th M5-P3) on U M-b (our analytical line for uranium). In each case, core and rim zones relatively depleted in U and Th (Th = 39,200 – 49,400 ppm; U = 5,700 – 8,000 ppm) are separated by an intervening zone of high U and Th (Th = 55,000 – 58,000 ppm; U = 8,100 – 8,200 ppm).

4. (U-Th)/He Methodologies

[7] Both conventional and laser microprobe (U-Th)/He methodologies require separate measurements for parent (U, Th, Sm) and daughter (He) elements, because there exists no single analytical instrument that can measure all of these elements with the abundance sensitivity and precision required for geochronology. Thus, all (U-Th)/He ages are the products of multiple analytical procedures, which we will describe here in order that the differences between conventional and laser microprobe implementations of the (U-Th)/He technique can be made clear.

4.1. Conventional (U-Th)/He Chronometry

[8] In conventional (U-Th)/He chronometry, single crystals are evaluated under high magnification transmitted-light microscopy for inclusions, fractures, breakage or other imperfections. Acceptable crystals are measured (in 3-D) and loaded into microcrucibles of Pt or Nb. This measurement, and the ejection correction derived from it are generally not considered to be significant in calculating (U-Th)/He ages, but the recent work of *Evans et al.* [2008] has demonstrated that measurements made by experienced analysts can vary by 4–9%, and in one case differed from a value calculated by computed microtomography by 24%. This suggests that grain measurement is a nonnegligible additional source of uncertainty that should be incorporated into final age error estimates for conventional (U-Th)/He.

[9] The measured crystals are then loaded into an ultrahigh vacuum laser chamber or resistance furnace and gently heated to release He. Care must be taken not melt the crystal, as vapor-phase loss of Th (and or U) may occur [*House et al.*, 2000]. Crystals are then retrieved and dissolved in concentrated acids for analysis of U, Th, and Sm, which is usually accomplished by isotope-dilution, inductively coupled plasma mass spectrometry. The resulting (U-Th)/He age must then be corrected for the alpha particles that are ejected from the crystal during nuclear decay. This correction is sensitive to the energy of the alpha particle, the physical model employed to calculate stopping distances, the composition and density of the mineral host, the size and shape of the crystal, as well as zoning and the presence of parent-rich inclusions. Such corrections can be in excess of 50% of the uncorrected age for small crystals, and any uncertainties in the correction should be (but often are not) propagated into the total uncertainty in the age.

[10] The end result of this effort is that each crystal can only yield one (U-Th)/He age, and the painstaking work required to find "perfect" crystals must be multiplied if replicate analyses are to be performed. It should be noted that the reasons for this degree of selectivity are multifold. Inclusions rich in parent elements (such as zircon or monazite) may contribute a significant fraction of radiogenic He to a relatively parent-element-poor host crystal, but the parent elements in the inclusion may not be accounted for if the inclusion is not dissolved along with the host. Inclusions can also represent a form of extreme zoning, which could result in erroneous alpha-ejection corrections: An inclusion that dominates the parent-element budget of the crystal (such as a zircon or monazite inclusion in apatite) would necessitate a ~50% alpha-ejection loss correction if located at the surface of the host, and a 0% correction if the inclusion was sufficiently far from the surfaces of the host crystal to prevent any alpha escape by recoil. Broken crystals (anhedral or subhedral fragments) are also likely to result in erroneous ejection corrections, as the original shape and size of the crystal is not easily estimated. At best the analysis of such grains results in larger, poorly constrained uncertainties, and at worst it results in calculated dates that contain no real age information. In the case of detrital samples, being selective about grain quality could skew the resulting age populations because different populations of crystals may have experienced varying transport conditions and distances that result in systematic textural differences.

4.2. Laser Microprobe (U-Th)/He

[11] For laser microprobe (U-Th)/He, crystals are mounted in epoxy or dental acrylic, and polished

by hand (to 0.05 μm grit) in order to produce a smooth, flat surface. This serves several purposes: First, the polishing exposes the interior of the crystal that is less likely to be affected by alpha-ejection-induced helium loss, obviating the ejection correction (and the associated error, which is difficult to quantify) which typically must be made to whole-grain (U-Th)/He ages [*Farley et al.*, 1996; *Hourigan et al.*, 2005]. Second, this polishing allows the internal parent element variations to be evaluated directly and with high fidelity. In most cases, qualitative mapping such as that provided by X-ray or backscattered-electron analysis is performed, followed by quantitative analysis by electron microprobe, secondary ion mass spectrometer, or other in situ technique. Recent developments in 3-D tomographic imaging of U and Th at the subgrain scale [*Evans et al.*, 2008] may lead eventually to high-resolution 3-D maps of parent elements within crystals, but even the knowledge of 2-D zoning provided by mapping polished grain interiors promotes judicious placement of laser microprobe analyses in order to avoid regions of particularly strong zoning, inclusions or other complications. Finally, careful polishing generates a flat and smooth surface to serve as a reference for measuring ablation pit volumes.

[12] After characterization, the crystals are repolished to remove the carbon coating required for electron microprobe analysis. The crystals are then remounted in indium, a necessary step because epoxy, dental acrylic, and other organic-rich potting materials are not compatible with the ultrahigh vacuum environment required for He analyses. Samples are then placed into the ultrahigh vacuum laser chamber with a sapphire or UV glass window (UV glass was used for the analyses in this paper) and ablated with a deep UV laser (such as the Lambda Physik excimer laser, operating at a nominal wavelength of 193 nm) to release He. Typical ablation pits are $\sim$20–100 μm in diameter, and 1–50 μm deep, depending on the He concentration and purpose of the measurement (sequential depth profiles versus single-age pits). Radiogenic helium released by ablation is spiked with a known amount of ^{3}He, purified by active metal getters, and measured by isotope dilution on a quadrupole mass spectrometer following the procedures outlined by *Boyce et al.* [2006]. Ablated volumes are then measured by optical interferometry or laser confocal microscopy, allowing He concentrations to be determined.

[13] In contrast to conventional (U-Th)/He, the effective spatial resolution of a few tens of microns

or less of the laser microprobe allows multiple measurements to be performed on individual crystals. In addition, the laser microprobe allows broken, irregular or included grains to be analyzed, further reducing the time required to find suitable crystals by relaxing quality constraints. The ability to date crystals of varying quality also reduces the risk of skewing ages in mixed populations of crystals such as detrital samples.

5. Results and Discussion

[14] Calculation of (U-Th)/He ages and uncertainties is accomplished by iterative application of a forward modeling Monte Carlo method and the ^{4}He production equation (commonly referred to as the "(U-Th)/He age equation") extended to include secular disequilibrium in the intermediate daughter products of ^{238}U, following a conceptualization similar to that of *Farley et al.* [2002]. This is discussed in detail below.

[15] Targeting regions of the core and intermediate zones away from the ejection depleted crystal surfaces, we were able to determine (U-Th)/He dates for 14 ablation pits in Crystal 1 and 7 pits in Crystal 2. Each pit had a diameter of $\sim$30 μm and a depth of $\sim$12–14 μm (inset of Figure 1), measured using a Carl Zeiss Instruments LSM 5 Pascal confocal laser microscope. Reflected laser source light is detected by confocal microscopy, providing depth resolution in addition to lateral resolution. Combined with a moving stage, this allows a surface to be mapped in high resolution, creating a nanoscale digital elevation model, from which volumes can be calculated. Nominal resolution of this instrument is $\sim$25 nm in the vertical direction, with a horizontal resolution of <0.25 μm. The uncertainty is this volume measurement as calculated from the voxel uncertainties would be negligible. However, the absolute accuracy of these measurements is unknown, because no "volume standards" exist for concavities such as ablation pits (and "bump-height standards" are not relevant for ablation pits given the reduced amount of laser light returning from pit bottoms). In addition, there is uncertainty derived from the assumptions regarding the flatness of the original surface from which the pit volume is subtracted. Because of this, we estimate the uncertainty of the pit volume at 5% (2σ), but we acknowledge that this is only an estimate and that future efforts to calibrate the precision and accuracy of pit volume measurements need to be made, preferably with multiple techniques and independent assessments of volume.
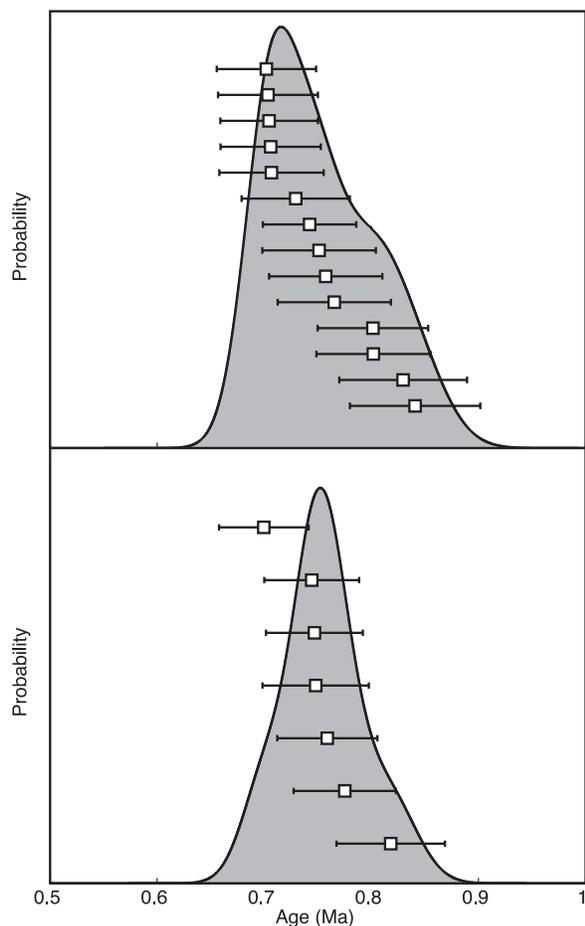
Figure 2. Probability distribution function of Nanga Parbat Laser microprobe (U-Th)/He ages, with sorted individual ages and 2σ uncertainties for crystals (top) 1 and (bottom) 2.

[16] In all cases, the pits were far enough from the crystal surfaces to avoid regions of extracrystalline alpha ejection, but some pits required minor corrections for zone-to-zone alpha exchange as described below, following the methodology of *Boyce and Hodges* [2005]. Although this correction results in a negligible change in the calculated mean age, it was performed for each spot, and an estimate of the increased uncertainty (geometric mean of concentrations on either side of a relevant zone boundary) from the correction was incorporated into the age calculation.

[17] Twenty-one of the twenty-two pits analyzed in the two monazite crystals yielded similar ages (Figure 2 and Table 1). Fourteen independent age determinations within Crystal 1 yield an error-weighted mean age of 746 ka and a mean uncertainty (2σ) of 51 ka (6.5%). The mean squared weighted deviation (MSWD) for the Crystal 1

mean age is 3.4, a value larger than that which might be explained simply by random experimental error if our estimates for the various error input parameters are correct [*Wendt and Carl*, 1991]. As a consequence, we multiplied the nominal uncertainty in the mean (two standard errors of the mean, here designated 2SE) by the square root of the MSWD [*Ludwig*, 2003] to arrive at a conservative estimate of 26,000 years (2SE) for the uncertainty in the error-weighted mean age of Crystal 1. Seven analyses of Crystal 2 yield a second mean age of 753 ± 33 ka (MSWD = 2.5), with one outlier analysis at 1.2 Ma which was rejected on both statistical grounds, and by an evaluation of the helium analysis, which exhibited an unusual gas evolution curve. It is the ability of the laser microprobe to generate multiple ages on individual crystals that enables us to robustly evaluate this single date as an outlier, a determination that would be difficult with the small replicate populations that typify conventional (U-Th)/He studies. Since the means for these two monazite crystals are statistically indistinguishable, we combined the 21 analyses to arrive at a mean age for both crystals of 748 ± 19 ka (2SE).

[18] We can make several first-order conclusions from the 21 laser microprobe analyses on these two crystals. First, we note that the both the internal and external reproducibilities are quite good for both crystals, with 95% confidence intervals of 3.5% and 4.4% within the crystals, and means that agree within 7,000 years. The lack of variation observed in cooling ages from these crystals is indicative of the rapid cooling that this sample must have experienced, which we discuss further below. However, the MSWD for all 21 analyses (2.9) is in excess of what would be expected if there was not scatter beyond our estimates of the uncertainties. Thus our ability to discern variations between individual spots is at best at the level of variations greater than ~7%, and it is likely that the true uncertainties are slightly larger than our estimates.

Table 1. U and Th Measurements for Each Crystal[a]

Domain	U	U 2σ	Th	Th 2σ	Sm	Sm 2σ
Crystal 1						
Core	7011	492	45719	1108	13584	1290
Middle	8209	540	57943	1294	14830	1282
Rim	6024	218	49376	576	16071	677
Crystal 2						
Core	7980	276	39176	504	15960	710
Middle	8101	257	55204	591	15968	607
Rim	5689	404	46835	1076	15169	1272

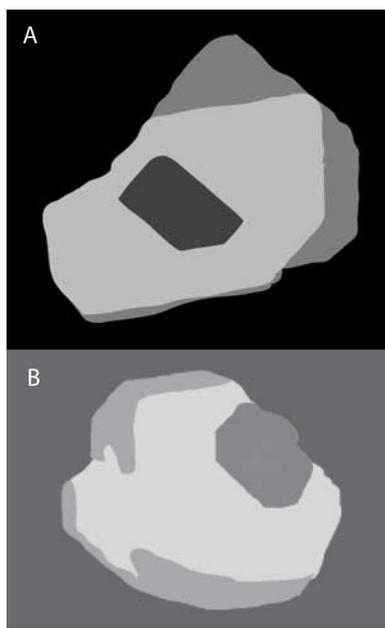[a] Uncertainties reported as two standard deviations from the mean.

Figure 3. Simplified U, Th, and Sm maps for recoil-based parent element modeling. Color scale is a function of concentration, chosen so that it mimics backscattered electron intensity: light (bright) grays are higher concentrations, while darker grays are relatively lower concentrations. Color scale is different for each element (see Figure 4 and Table 2). (a) Field of view is $\sim$350 μm $\times$ $\sim$260 μm. (b) Field of view is $\sim$485 μm $\times$ $\sim$360 μm.

5.1. Calculating Effective Parent Element Concentrations due to Ejection Redistribution

[19] The relevant parent element concentrations for a given spot on the map are not the U, Th, and Sm concentrations at/within that volume, but are rather a function of the parent element distribution in the region surrounding (and in some cases, including) the volume being analyzed for He. This is counterintuitive for scientists accustomed to other in situ geochronologic techniques where the parent and daughter elements are located in approximately the same location. This is not true of (U-Th)/He because the alpha particles in a given region were actually (in the case where diffusion is negligible) generated roughly one ejection distance away and ejected (randomly) to that spot. In the case of a laser pit width that is less than the ejection distance, very little (theoretically none) of the He in the pit was generated by parent elements in the same volume because those U, Th, and Sm were ejecting all of their He outside of the pit. Therefore we are justified, in many cases, in making measurements of the parent elements outside of the ablation pit. This implies that zoning in the region surround-

ing the ablation pit may affect the He content within the pit. Therefore, the importance of the alpha redistribution within zoned crystals is important to evaluate. In order to properly account for alpha recoil from a three-dimensional distribution of parent elements, we must create a model to calculate the "effective" parent element concentrations for each spot on the map of the crystal.

[20] The first step is to create a simplified map of the parent element concentrations in each crystal using the discrete spot analyses of U, Th, and Sm concentrations and the backscattered electron maps from the electron microprobe (Figure 3). Each crystal is defined to have three homogeneous zones, with concentrations defined by electron microprobe analysis (Table 1). The map of the crystal is surrounded by a zero boundary condition, as the concentrations of U, Th, and Sm outside the crystal were considerably ($\sim$1000$\times$) less than the concentrations in the crystal. This assumption is likely true for the major mineral phases (feldspars, quartz, etc.) found in the leucogranite from which these monazites were derived, and is the same assumption made for conventional alpha-ejection corrections [*Farley et al.*, 1996].

[21] Following the model of *Boyce and Hodges* [2005], we calculate the "effective" concentration of each parent element at each node in the elemental map by averaging all the parent element concentrations located one ejection distance away from the node of interest. We do this because these are the effective (or apparent) amounts of the parent elements that result in the amount of He observed at that node. Because this is a three-dimensional problem, we assume that there is no variation out of the plane of the map, a simplification necessary because the true compositions are not available as a function of depth. This assumption is less likely to effect the calculations for shallow pits in crystals with relatively long-wavelength zoning, where changes in composition over the depth of a pit are likely to be minimal. In order to account for out-of-plane effects, we calculate the position in the plane corresponding to the vertical projection of the points on the surface of an imaginary sphere centered on the node of interest. By sampling the sphere at $\sim$10° increments in azimuth and inclination, and finding the nearest Cartesian grid points, we can map 3600 points lying near the surface of the sphere on to the map plane. The elemental concentrations for those points are then averaged, the value stored, and the process repeated for all points in the map.
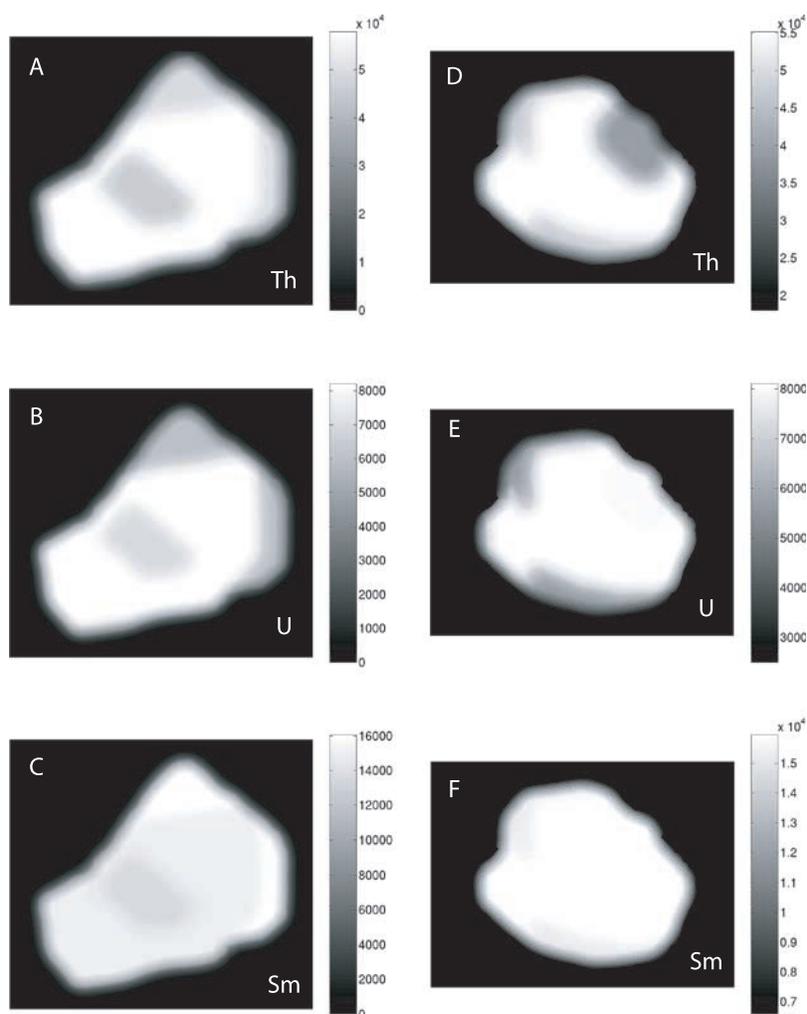
Figure 4. Alpha-recoil corrected maps of effective parent concentrations: (a and d) Th, (b and e), U, and (c and f) Sm. Note that zone boundaries modeled as sharp step functions in true U-Th-Sm concentrations are gradational in "effective concentration" (which is what controls He production). Sizes as in Figure 3. Scale bars are concentration in ppm.

[22] The results of the model are shown in Figure 4 for each of the parent elements. As one would expect, regions near the edge of a crystal have a low effective parent composition, reflecting the fact that there is no contribution to nodes near the edge from any neighboring nodes outside the crystal. Regions of the crystal near zone boundaries also show effects of alpha ejection on effective parent element concentrations. Any node near a boundary will receive ^{4}He from both sides of the zone, resulting in an effective parent element concentration that reflects the partial contribution from each zone.

[23] Effective concentrations of U, Th, and Sm for a given analysis are calculated by averaging all the nodes within each ablation pit (Table 2). Uncertainties are propagated as averages, using the

geometric mean of the uncertainties of the individual zones, except in cases where spots were completely contained within one zone, in which case the uncertainty on the concentrations from only that zone was propagated into the age calculation.

5.2. Secular Equilibrium and (U-Th)/He Ages

[24] For very young samples such as these from Nanga Parbat, one must assess the possible importance of secular equilibrium on the production of uranium daughter products such as He and Pb [*Farley et al.*, 2002; *Schärer*, 1984]. Secular disequilibrium is typically defined by estimated isotope ratios at the time of crystallization, or by measured isotope ratios at present. For the monazites dated in this study, any excess ^{230}Th initially

Table 2. Data Used to Calculate Laser Microprobe (U-Th)/He Ages, Along With Those Ages and Uncertainties[a]

Spot	^{4}He (mols $\times 10^{-15}$)	^{4}He (2σ)	Volume (μm^3)	Volume (2σ)	U (ppm)	U (2σ)	Th (ppm)	Th (2σ)	Sm (ppm)	Sm (2σ)	Age (ka)	Age (2σ)	Age (2 SE)
1a	2.498	0.064	6002	296	6933	381	52984	899	15555	970	765.4	52	
1b	2.452	0.093	5772	289	6513	381	49931	899	15159	970	829.7	61	
1c	2.660	0.08	6228	311	8130	381	57529	899	14875	970	703.5	47	
1d	2.604	0.087	6028	304	8208	381	57922	899	14831	970	706	47	
1e	2.593	0.071	6195	304	6245	381	48911	899	15373	970	840.9	60	
1f	2.473	0.12	5830	292	8092	381	56609	899	14710	970	706.8	48	
1g	2.363	0.068	5908	299	7555	381	51059	899	14094	970	729.4	50	
1h	2.173	0.063	5679	281	7116	381	46998	899	13694	970	751.2	53	
1i	2.250	0.074	5604	285	7322	381	49270	899	13908	970	757.4	53	
1j	2.864	0.076	5873	293	8154	381	57628	899	14861	970	801.4	53	
1k	2.479	0.081	5801	294	8155	381	57316	899	14817	970	704.5	47	
1l	2.559	0.069	5977	299	8194	381	57653	899	14814	970	702	45	
1m	2.516	0.077	5536	277	8209	270	57943	647	14830	641	742.3	44	
1n	2.480	0.062	5171	259	8022	381	56590	899	14808	970	801.9	53	
Crystal 1 mean[b]											746	49	26
2a	2.540	0.077	5787	289	8082	276	55084	664	15962	789	744.3	46	
2b	2.497	0.08	5886	291	7480	276	52982	664	15762	789	758.9	46	
2c	2.477	0.068	5630	282	7058	276	51543	664	15623	789	818.1	49	
2d	2.653	0.064	6103	305	7941	276	54521	664	15915	789	746.8	44	
2e	2.553	0.067	6128	306	8041	276	47359	664	15964	789	775.2	48	
2f	3.657	0.098	6149	307	7965	276	39788	664	15921	789	1225.3	79	
2g	2.636	0.079	6400	320	8071	276	54969	664	15958	789	699.6	42	
2h	2.198	0.073	6005	307	6143	276	48070	664	15245	789	748	48	
Crystal 2 mean[c]											753	36	33
Crystal 1 and 2 mean[d]											748	44	19

[a] U, Th, and Sm concentrations reported here are effective concentrations, derived from the modeling of the values in Table 1, as described in the text.
[b] Mean of 7 spots on crystal 1 (N = 7). Two standard deviations of the mean and two standard errors of the mean are 6.5% and 3.5%, respectively.
[c] Mean of 14 spots on crystal 2 (N = 14). Two standard deviations of the mean and two standard errors of the mean are 4.8% and 4.4%, respectively.
[d] Mean of 21 spots for both crystals (N = 21). Two standard deviations of the mean and two standard errors of the mean are 5.9% and 2.5%, respectively.

present has decayed over the $\sim$16–20 half-lives since crystallization at 1.2–1.4 Ma, and cannot be measured. Therefore we use estimated initial ^{230}Th excesses based on Th/U ratios determined for melts in equilibrium with monazites from the host rock, which for these rocks are 0.41 – 1.11 [*Crowley et al.*, 2005]. However, unlike for U-Pb geochronology, the amount of secular equilibrium present at the time of crystallization does not immediately impact the accumulation of He (assuming that crystallization occurs well above the He closure temperature of the crystal). The amount of time in between crystallization and the start of the (U-Th)/He clock (the "cooling interval") decreases the effect of disequilibrium, as the system returns to secular equilibrium during that interval. The correction for ^{4}He production by "excess" ^{230}Th incorporated into the monazite structure during crystallization is in all cases here less than 5,000 years. Although this value is much smaller than the uncertainty in the ages, this correction has been applied, and the additional uncertainty stemming

from this correction has been incorporated into the total uncertainty in age.

5.3. Cooling and Exhumation Rates From Thermochronometry

[25] The simple fact that the weighted mean cooling age determined for these monazites is $\sim$750 ka suggests that cooling must have been quite rapid, given the lack of evidence for late heating that could have caused He loss. We can model the cooling compatible with this rock, for a range of diffusion coefficients for helium in monazite consistent with published experimental data [*Boyce et al.*, 2005; *Farley*, 2007], and the dimensions of our grains. The Ce-rich compositions of the Nanga Parbat monazites lead to an estimated T_C of $\sim$250°C for both crystals. In Figure 5 we have plotted the range of permissible T_C values (including diffusion coefficient measurement uncertainties) against the observed distribution of ages, with superimposed contours of mean cooling rate in K/Ma. These cooling rates are not model dependent
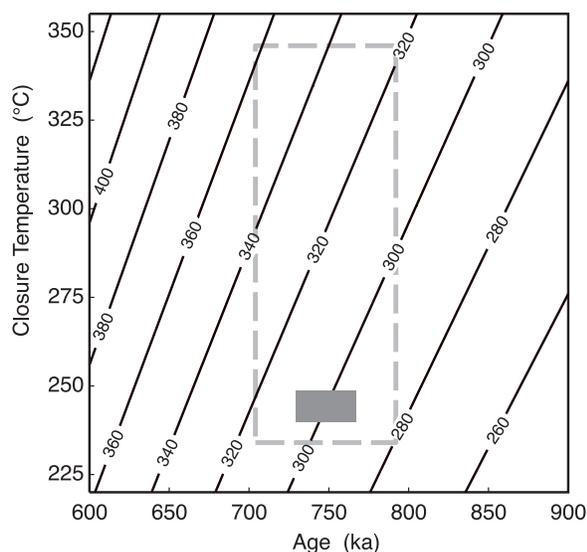
Figure 5. Contours of mean cooling rate (K/Ma) superimposed over the range of experimentally determined T_C versus the two standard deviation distribution of observed (U-Th)/He ages for both crystals. Large gray dashed rectangular box delineates the range of cooling rates compatible with the ages measured here and the entire range of experimentally determined T_C for natural and synthetic monazites of all studied compositions [Boyce et al., 2005; Farley, 2007]. Small gray scale rectangle covers range of cooling rates that are consistent with synthetic monazite of this composition (Ce-monazite of Farley [2007], with an activation energy of 196 kJ/mol and preexponential factor of 200 cm²/s) and the two standard error of the mean age distribution determined in this study.

because they are mean values, representing an average over the (U-Th)/He cooling lifetime of the monazites, roughly comparable to the cooling age of 0.75 Ma. Considering the entire range of T_C values that would be calculated for monazites of this size using all the available He diffusion data in the literature, and the observed two standard deviation distribution of cooling ages, we can constrain the cooling rate experienced by this rock to between 280 K/Ma and 360 K/Ma (dashed gray box, Figure 5). However, the most likely cooling rates consistent with the known composition of this monazite and the best estimate of the uncertainty on the mean age (two standard errors of the mean) lie in a much narrower range, between 290 K/Ma and 310 K/Ma. The ages determined here, and the commensurate rapid cooling, are not only consistent with (younger than) the U-Pb geochronology determined for this same sample, but also in a more regional sense with the prior constraints for cooling at Nanga Parbat [Winslow et al., 1996]. Figure 6 is a compilation of preexisting fission track (apatite

and zircon) and $^{40}Ar/^{39}Ar$ (biotite and muscovite) data from Nanga Parbat, along with the (U-Th)/He data from this study. The (U-Th)/He data is consistent with the regional trend of young ages, including apatite fission track ages that are within error of zero age [Treloar et al., 2000]. The fact that the (U-Th)/He ages from this study err slightly on the "young" side of the trend is likely a result of sampling bias, specifically the difficulty of comparing ages from one sample with dozens of others in a geologically complex region. It should also be noted that the mean (U-Th)/He age here is within two standard deviations of the population of both apatite and zircon fission track ages, and just outside the 2σ envelope for $^{40}Ar/^{39}Ar$ of biotite. The take-home message is that a very young age such as that determined here is not unreasonable considering the thermochronologic context provided by previous workers.

[26] Converting cooling rates to exhumation rates is often the ultimate goal of performing thermochronology, and this requires modeling that is
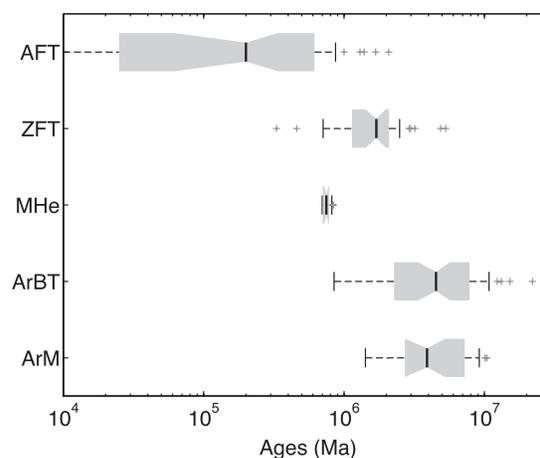

Figure 6. Box plot of thermochronologic data for the Nanga Parbat massif from Zeitler [1985], Winslow et al. [1994], Treloar et al. [2000], George et al. [1995], and Whittington [1996]. Width of gray boxes indicates range of upper and lower quartile from the median; notch indicates 95% confidence estimate (for comparing medians sans uncertainties). Whiskers are two standard deviations from the mean, and crosses indicate data that lie outside the 2σ range. Data are arranged (top to bottom) in approximate order from low to high closure temperature. Abbreviations: AFT (apatite fission track), ZFT (zircon fission track), MHe (monazite (U-Th)/He), ArBT ($^{40}Ar/^{39}Ar$ biotite), ArM ($^{40}Ar/^{39}Ar$ muscovite). The very small range in (U-Th)/He ages from this study, relative to the other data from the literature, is a function of the (U-Th)/He data being limited to only one sample location.
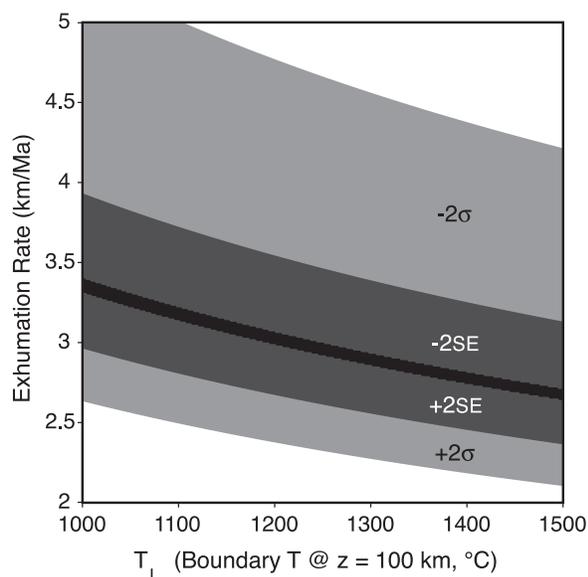
Figure 7. Model exhumation rates for the range of literature T_C values [*Farley*, 2007], measured (U-Th)/He ages (this paper), and thermal parameters, as implemented by *Braun et al.* [2006]. Gray scale regions indicate erosion rates compatible with the mean age (black line), the mean age $\pm 2\sigma$ (light gray), and the mean age $\pm 2SE$ (dark gray). While not intended as a rigorous model of exhumation at Nanga Parbat, this result does demonstrate the improved model constraints that can result from the increased precision provided by multiple analyses using the laser microprobe.

subject to many assumptions regarding the initial and boundary conditions as well as material properties of crust. The increased precision of laser microprobe (U-Th)/He ages can help constrain exhumation to a narrower range of possible models given all the other assumptions required. As an example, here we can use the simplified 1-D advection-diffusion model of *Braun et al.* [2006] to predict what exhumation rates are compatible with the range of possible T_C values and (U-Th)/He ages determined for Nanga Parbat monazites. Exhumation rates (Figure 7) compatible with the mean (U-Th)/He age of these monazites vary from ~2.7 km/Myr for "warmer" models (thermal boundary layer = 1500°C at 100 km) to ~3.4 km/Myr for "cooler" models (thermal boundary layer = 1000°C). Considering the full $\pm 2\sigma$ uncertainty in the ages a range of possible T_C for these samples would result in a range of model exhumation rates from ~2.1 km/Myr to ~6 km/Myr. However, using the $\pm 2SE$ uncertainty in the mean (U-Th)/He age (still including the range of T_C values) yields a narrower range of possible exhumation rates from ~2.5 km/Ma to ~3.9 km/Ma. Note that our ability to more tightly constrain the

range of permissible exhumation rates derives directly from the low uncertainties of the (U-Th)/He data presented here. These low uncertainties were achieved because we were able to combine a large number of dates for a single rock sample. Compared to conventional (U-Th)/He dating of single crystals, laser microprobe (U-Th)/He dating provides a distinct advantage in studies that require the kind of high precision afforded by large numbers of replicate analyses.

5.4. Cooling Profiles by Laser Microprobe (U-Th)/He

[27] During slow cooling, one would expect a internal age gradient from core to rim, reflecting the increased probability with which He near the edges of crystals will escape as a result of the random walks of diffusion. This commonly portrayed as a variation in closure temperature from core to rim [*Dodson*, 1986], and implies that a large portion of the temperature-time history of a rock can be obtained from a single crystal. In the case of a slowly cooled rock, one should be able to measure detectable differences in age between core and rims of single crystals, and thereby constrain multiple (T, t) points [*Hodges et al.*, 1994; *Hodges and Bowring*, 1995]. With the submicron resolution of the Excimer laser in depth profiling mode, obtaining a near-continuous thermal history should be possible. However, in the case of a quickly cooled rock, one would expect a minimal gradient within the crystal, except that caused by alpha ejection or zoning in parent elements. We can model the age gradient we would expect to have formed in these crystals if they were crystallized at 1.5 Ma @ ~700°C, and cooled to produce a closure age for He in monazite of ~750 ka. To do so we use HeFTy [*Ketcham*, 2005], a program for forward or inverse modeling of thermal histories constrained by thermochronometry. In doing so, we discover that the total range in age observed in the inner region of the crystal (away from the ejection-depleted rim) is never more than ~12% relative to the maximum age in the core of the crystal. As all of our analyses are within this inner region, and the scatter of the data is on the order of the same size as the variations predicted ($\pm 6\%$ at two standard deviations from the mean), our inability to resolve the gradient is consistent with this model.

[28] Although in this sample we are limited by scatter in the data (in large part) due to the young age of the sample, this study suggests that directly

imaging intracrystalline ^{4}He variations in accessory minerals using laser ablation should be feasible, especially given that conventional and laser microprobe (U-Th)/He ages have been demonstrated to agree within 1.3% for older standard materials. For very rapidly cooled samples with young ages and limited ^{4}He diffusive-loss zoning (such as this example from Nanga Parbat, where the predicted spread in age in the core is only ~100 ka), the laser microprobe offers an opportunity to produce numerous replicate analyses in a short time, increasing the effective analytical precision to levels comparable to the most precise conventional (U-Th)/He results. For more slowly cooled samples, where the internal age gradient is larger and the mean age is greater (making it easier to generate analyses with reduced scatter, relative to the ages determined), it should be possible to directly image those age gradients and invert them for thermal histories. The high spatial resolution of this technique also permits effectively nondestructive thermochronology of rare samples (such as meteorites or lunar samples).

[29] Of special importance to future applications is the capability of using the excimer laser for depth profiling with a nominal vertical resolution of ~0.1 μm (based on the theoretical limit of the depth of a single laser pulse). A more realistic and immediately obtainable resolution of ~1 μm could easily be achieved on monazite on the 5–10 Ma age range with no improvements in analytical abilities, as older samples have near-proportionally higher ^{4}He contents, permitting smaller ablation volumes. Advances in ion-counting mass spectrometry are likely to increase our effective resolution with respect to measurement uncertainty, as they permit increased confidence in measurements of small amounts of He. For example, recent work at Arizona State University has demonstrated that measurement errors of better than 1.5% can be obtained on magnetic-sector mass spectrometers using a secondary electron multiplier for gas loads on the order of 10^{-11} cc ^{4}He. This is approximately two orders of magnitude less ^{4}He than is required for the same size error using a quadrupole mass spectrometer such as was used for this study (M. van Soest, personal communication, 2008). By combining high-resolution depth profiles of ^{4}He concentration with appropriate production-ejection-diffusion models [*Ketcham*, 2005], it should be possible to develop extremely detailed reconstructions of the thermal evolution of appropriate samples for tectonic and landscape evolution studies. In addition, the rapid throughput permitted by

laser microprobe (U-Th)/He can be used to generate the large two- and three-dimensional data coverage that would be well suited to interpreting three-dimensional thermokinetic models.

Acknowledgments

References

Boyce, J., et al. (2006), Laser microprobe (U–Th)/He geochronology, *Geochim. Cosmochim. Acta*, *70*(12), 3031–3039, doi:10.1016/j.gca.2006.03.019.

Boyce, J. W., and K. V. Hodges (2005), U and Th zoning in Cerro de Mercado (Durango, Mexico) fluorapatite: Insights regarding the impact of recoil redistribution of radiogenic ^{4}He on (U–Th)/He thermochronology, *Chem. Geol.*, *219*, 261–274, doi:10.1016/j.chemgeo.2005.02.007.

Boyce, J. W., K. V. Hodges, W. J. Olszewski, and M. J. Jercinovic (2005), He diffusion in monazite: Implications for (U-Th)/He thermochronometry, *Geochem. Geophys. Geosyst.*, *6*, Q12004, doi:10.1029/2005GC001058.

Braun, J., et al. (2006), *Quantitative Thermochronology: Numerical Methods for the Interpretation of Thermochronological Data*, Cambridge Univ. Press, New York.

Craw, D., et al. (1997), Geochemistry of a dry steam geothermal zone formed during rapid uplift of Nanga Parbat, northern Pakistan, *Chem. Geol.*, *142*(1–2), 11–22, doi:10.1016/S0009-2541(97)00071-5.

Crowley, J. L., et al. (2005), U-Th-Pb systematics of monazite, xenotime, and zircon from Pleistocene leucogranites at Nanga Parbat (Pakistan Himalaya), *Geochim. Cosmochim. Acta*, *69*, A8.

Dodson, M. H. (1973), Closure temperature in cooling geochronologic and petrologic systems*Contrib. Mineral. Petrol.*, *40*, 259–274, doi:10.1007/BF00373790.

Dodson, M. H. (1986), Closure profiles in cooling systems, *Mater. Sci. Forum*, *7*, 145–154, doi:10.4028/www.scientific.net/MSF.7.145.

Evans, N., et al. (2008), Application of X-ray micro-computed tomography in (U-Th)/He thermochronology, *Chem. Geol.*, *257*(1–2), 101–113, doi:10.1016/j.chemgeo.2008.08.021.

Farley, K. A. (2002), (U-Th)/He dating: Techniques, calibrations, and applications, in *Noble Gasses*, edited by D. P. Porcelli et al., pp. 819–843, Mineral. Soc. of Am., Washington, D. C.

Farley, K. A. (2007), He diffusion systematics in minerals: Evidence from synthetic xenotime and zircon structure phosphates, *Geochim. Cosmochim. Acta*, *71*, 4015–4024, doi:10.1016/j.gca.2007.05.022.

Farley, K. A., et al. (1996), The effects of long alpha-stopping distances on (U-Th)/He ages, *Geochim. Cosmochim. Acta*, *60*, 4223–4229.

Farley, K. A., et al. (2000), (U-Th)/He dating of quaternary tephras and lavas, *Geol. Soc. Am. Abstr. Programs*, *32*, 325.

Farley, K. A., et al. (2002), The effects of secular disequilibrium on (U-Th)/He systematics and dating of Quaternary volcanic zircon and apatite, *Earth Planet. Sci. Lett.*, *201*, 117–125.

George, M., et al. (1995), Isotopic constraints on the cooling history of the Nanga Parbat-Haramosh Massif and Kohistan Arc, western Himalaya, *Tectonics*, *14*(2), 237–252, doi:10.1029/94TC02906.

Hodges, K. V., and S. A. Bowring (1995), $^{40}Ar/^{39}Ar$ thermochronology of isotopically zoned micas: Insights from the southwestern USA Proterozoic orogen, *Geochim. Cosmochim. Acta*, *59*(15), 3205–3220, doi:10.1016/0016-7037(95)00209-I.

Hodges, K. V., et al. (1994), $^{40}Ar/^{39}Ar$ age gradients in micas from a high-temperature-low-pressure metamorphic terrain: Evidence for very slow cooling and implications for the interpretation of age spectra, *Geology*, *22*(1), 55–58, doi:10.1130/0091-7613(1994)022<0055:AAAGIM>2.3.CO;2.

Hourigan, J., et al. (2005), U-Th zonation-dependent alpha-ejection in (U-Th)/He chronometry, *Geochim. Cosmochim. Acta*, *69*(13), 3349–3365, doi:10.1016/j.gca.2005.01.024.

House, M. A., et al. (1998), Dating topography of the Sierra Nevada, California, using apatite (U-Th)/He ages, *Nature*, *396*, 66–69, doi:10.1038/23926.

House, M. A., et al. (2000), Helium chronometry of apatite and titanite using Nd-YAG laser heating, *Earth Planet. Sci. Lett.*, *183*, 365–368.

Jercinovic, M. J., and M. L. Williams (2005), Analytical perils (and progress) in electron microprobe trace element analysis applied to geochronology: Background acquisition, interferences, and beam irradiation effects, *Am. Mineral.*, *90*, 526–546, doi:10.2138/am.2005.1422.

Ketcham, R. A. (2005), Forward and inverse modeling of low-temperature thermochronometry data, in *Low-Temperature Thermochronology: Techniques, Interpretations, Applications*, *Rev. Mineral. Geochem.*, vol. 58, edited by P. W. Reiners and T. A. Ehlers, pp. 275–314, Mineral. Soc. of Am., Washington, D. C.

Koons, P. O., et al. (2002), Mechanical links between erosion and metamorphism in Nanga Parbat, Pakistan Himalaya, *Am. J. Sci.*, *302*, 749–773.

Ludwig, K. R. (2003), Mathematical-statistical treatment of data and errors for $^{230}Th/U$ geochronology, *Rev. Mineral. Geochem.*, *52*, 631–656, doi:10.2113/0520631.

McDowell, F. W., et al. (2005), A precise $^{40}Ar-^{39}Ar$ reference age for the Durango apatite (U–Th)/He and fission-track dating standard, *Chem. Geol.*, *214*, 249–263, doi:10.1016/j.chemgeo.2004.10.002.

Min, K. (2005), Low-temperature thermochronometry of meteorites, *Rev. Mineral. Geochem.*, *58*(1), 567–588, doi:10.2138/rmg.2005.58.21.

Reiners, P. W. (2002), (U-Th)/He chronometry experiences a renaissance, *Eos Trans. AGU*, *83*(3), 21, doi:10.1029/2002EO000012.

Schärer, U. (1984), The effect of initial ^{230}Th disequilibrium on young U-Pb ages: The Makalu case, Himalaya, *Earth Planet. Sci. Lett.*, *67*, 191–204, doi:10.1016/0012-821X(84)90114-6.

Tagami, T. (2003), (U–Th)/He geochronology of single zircon grains of known Tertiary eruption age, *Earth Planet. Sci. Lett.*, *207*(1–4), 57–67, doi:10.1016/S0012-821X(02)01144-5.

Treloar, P. J., and D. C. Rex (1990), Cooling and uplift histories of the crystalline thrust stack of the Indian Plate internal zones west of Nanga Parbat, Pakistan Himalaya, *Tectonophysics*, *180*, 323–349, doi:10.1016/0040-1951(90)90317-2.

Treloar, P. J., et al. (2000), Geochronological constraints on the evolution of the Nanga Parbat syntaxis, Pakistan Himalaya, in *Tectonics of the Nagna Parbat Syntaxis and the Western Himalaya*, edited by M. A. Khan et al., *Geol. Soc. Spec. Publ.*, 137–162.

Wendt, I., and C. Carl (1991), The statistical distribution of the mean squared weighted deviation, *Chem. Geol.*, *86*, 275–285.

Whittington, A. G. (1996), Exhumation overrated at Nanga Parbat, northern Pakistan, *Tectonophysics*, *260*, 215–226.

Winslow, D. M., et al. (1994), Direct evidence for a steep geotherm under conditions of rapid denudation, Western Himalaya, Pakistan, *Geology*, *22*, 1075–1078, doi:10.1130/0091-7613(1994)022<1075:DEFASG>2.3.CO;2.

Winslow, D. M., P. K. Zeitler, C. P. Chamberlain, and I. S. Williams (1996), Geochronologic constraints on syntaxial development in the Nanga Parbat region, Pakistan, *Tectonics*, *15*(6), 1292–1308.

Zeitler, P. K. (1985), Cooling history of the NW Himalaya, Pakistan, *Tectonics*, *4*, 127–151, doi:10.1029/TC004i001p00127.

Zeitler, P. K., et al. (1982), Fission track evidence for Quaternary uplift of the Nanga Parbat region, Pakistan, *Nature*, *298*, 255–257, doi:10.1038/298255a0.

Zeitler, P. K., et al. (1989), Geochronology and temperature history of the Nanga Parbat-Haramosh massif, Pakistan, in *Tectonics of the Western Himalayas*, edited by L. L. Malinconico and R. J. Lillie, *Spec. Pap. Geol. Soc. Am.*, *232*, 1–22.

Zeitler, P. K., et al. (2001), Crustal reworking at Nanga Parbat, Pakistan: Metamorphic consequences of thermal-mechanical coupling facilitated by erosion, *Tectonics*, *20*(5), 712–728, doi:10.1029/2000TC001243.